Graphene nanostrip transverse magnetic dual-channel refractive index sensor

MD. MAHBUB HOSSAIN [ID] **AND MUHAMMAD ANISUZZAMAN TALUKDER**[*] [ID]

Department of Electrical and Electronic Engineering, Bangladesh University of Engineering and Technology, Dhaka 1205, Bangladesh
[*]*anis@eee.buet.ac.bd*

Abstract: Generally, transverse magnetic (TM) polarization-based surface plasmons (SPs) are excited in plasmonic devices. While the transverse electric (TE) modes can be excited in graphene up to the visible frequency range, TM modes can be supported only from terahertz to the mid-infrared region. We show that graphene TM modes can be excited in the visible spectrum by applying a suitable voltage to the graphene layer and using an appropriate interfacing dielectric layer thickness. Furthermore, utilizing this TM mode, we propose a dual-channel refractive index sensor where the same analyte can be injected into the two channels for significantly sensitive detection of the analyte, or two different analytes can be injected into the two channels for their simultaneous detection. The proposed sensor exploits two graphene layers, one with nanostrip arrays, for efficient TM mode excitation. The nanostrips in the first graphene layer scatter the incoming radiation to the second, generating TM modes at both layers. The proposed dual-channel sensor shows 2530 degrees/RIU peak sensitivity when the sensing channels have the same analyte. The graphene nanostrips-based sensor will be a promising alternative to the traditional Kretschmann arrangement and significantly impact biosensing and refractive index sensing without needing noble metal in the structure.

1. Introduction

Surface plasmons (SPs) propagate at a metal–dielectric interface, confining light in sub-wavelength dimensions [1]. During the past decade, SPs excited at a metal–dielectric interface have drawn significant interest for their applications in biosensing. However, metals are inherently lossy, and hence the propagation length of metal-based SPs is limited. In addition, the direct excitation of metal-based SPs is impossible due to the wave vector mismatch between the incident light and SPs and the difficulty in altering the dielectric properties to overcome such a mismatch [2]. On the other hand, plasmons excited at graphene–dielectric interface show controllable electromagnetic (EM) properties, comparatively low loss, and intense light absorption [3]. As a result, plasmons excited in graphene are promising alternatives for metal-based SPs in many areas of photonic and plasmonic devices, from mid-infrared (MIR) to terahertz (THz) wavelength region [4–7]. In addition, characteristics of graphene plasmons strongly depend on the substrate's physical and geometrical parameters and can be tailored as per requirement [8].

Graphene shows an extraordinary property variation from dielectric to metallic responses at energies near $\hbar\omega \approx 2E_f$, where E_f is the Fermi energy, $\hbar$ is the reduced Planck's constant, and ω is the angular frequency [9]. In graphene, E_f can be efficiently controlled by doping [9,10]. Graphene conductivity (σ_g), especially the imaginary part, Im(σ_g), changes sign from positive to negative when $\hbar\omega > 2E_f$, with the minimum at $\hbar\omega = 2E_f$ [11,12]. The change of sign occurs since the electric field reverses the direction of induced current [13]. The negative sign of Im(σ_g) confirms the presence of the transverse electric (TE) mode in graphene [12]. However, the TE mode's dispersion relation is very close to the light line, and it cannot confine the incident light sufficiently [13]. On the other hand, when Im(σ_g)>0, the transverse magnetic (TM) mode is

supported in graphene [13]. Furthermore, graphene does not support TE and TM modes in the same wavelength region [2]. Graphene's optical characteristics are changed by applying an electrical voltage, which modulates the plasmon resonance in the metal nanostructures [14,15]. Applying a suitable gate voltage (V_g) to the graphene and using an appropriate interfacing dielectric layer thickness allows the TM mode to be excited at a desired wavelength [16], allowing designing optoelectronic and plasmonic devices in optical frequency.

When $\hbar\omega < 1.667E_f$, graphene shows metallic responses with a positive imaginary part of σ_g, supporting TM modes and ensuring strong light confinement with huge wave vectors [17]. However, graphene TM modes can reach the MIR range, whereas graphene TE modes up to the visible range [18]. In addition, TM modes show collective electron oscillations; therefore, the real part of ε_g must be negative to excite them in graphene [19]. TM modes have been experimentally observed in graphene micro-ribbon arrays, infrared nano-imaging, nanoscopy, and sub-wavelength gratings from THz to infrared (IR) wavelength range [2,20,21]. Besides, when photon energies (E_p) are $>2E_f$, mono-layer graphene shows 2.3% light absorption, which limits the conversion from light to the electronic signals in a graphene layer [22].

The Kretschmann-based angular interrogation method is generally used to create SPs, showing a high signal-to-noise ratio. However, the resonance angle shifting must be significant for enhanced sensor performance. The sensitivity of a Kretschmann configuration sensor is usually low, ~200 degrees/RIU (refractive index unit) [23]. It is possible to increase the sensitivity by decreasing the refractive index of the prism material, although this approach reduces the detection accuracy [23]. To overcome the low sensitivity problem, several research groups have proposed various modified structures [24–29], e.g., metal nano-grooves, graphene/hexagonal boron nitride (hBN) nanoribbons, metal/dielectric/metal-based plasmonic sensors to decrease the reflected light intensity. Furthermore, a silver (Ag)-gold (Au) grating SPR-based sensor has shown a maximum 346 degrees/RIU sensitivity [30]. However, these SPR sensors are not prism-based, which are extensively used commercially [31]. Besides, graphene nanostrips in Au-aluminium (Al)-based SPR sensors have shown a maximum 165 degrees/RIU sensitivity and 164.28 RIU^{-1} figure-of-merit (FoM), respectively [32]. However, the effects of nanostrip geometry, such as thickness and length, on sensing performance have yet to be analyzed. Recently, an SPR sensor based on Au grating, where SPR and localized SPR (LSPR) coupling is proposed, achieved a maximum sensitivity of 397.3 degrees/RIU [33].

On the other hand, TM modes in doped monolayer graphene on a dielectric layer have been investigated through attenuated total reflectance (ATR) based technique in THz wavelength [34]. Likewise, graphene-based constructions using ATR have been proposed for polarizers and switches by adjusting V_g [35,36]. In addition, graphene can be sandwiched between different dielectric materials, such as SiO_2 and Si layers, to control E_f and the electron density (n_g) [8,37,38]. By applying a suitable V_g, n_g can be increased. When $n_g \gtrsim 4\times10^{14}$ cm^{-2}, $E_f = 2.3$ eV [2,39]. Furthermore, the TM mode properties in graphene strongly depend on the relative permittivity (ε_r) and thickness (d) of SiO_2 [37]. However, it is observed that ε_r of SiO_2 is comparatively small. The only parameter to increase the E_f is the SiO_2 thickness. Alternatively, ZnO can be considered instead of SiO_2 due to its high ε_r [40].

This work shows that TM modes can be excited in graphene using the ATR method in the visible spectrum without needing a noble metal. We show that graphene optical properties can be effectively tuned by changing the thickness of the interfacing dielectric layer (d_{ZnO}) and V_g. We use the Kubo analytical model to determine the graphene layer's optical properties. The proposed sensor uses dual channels for refractive index sensing, where graphene nanostrips are placed in the first layer. These nanostrips scatter the incident light to a second graphene layer through several intermediate dielectric layers. Our proposed dual-channel sensor shows a maximum sensitivity of 2530 degrees/RIU when both sensing channels have the same refractive index.

This paper is organized as follows: Section 2 presents the proposed dual-channel sensor configuration. Section 3 describes the optical properties of different materials. We discuss the numerical method to solve Maxwell's equations by the finite difference time domain (FDTD) technique in Sec. 4. We present the dynamics of incident light with the sensor structure in Sec. 5 and the sensing performances of the proposed dual-channel sensor in Sec. 6. Section 7 concludes the findings of this work.

2. Proposed dual-channel sensor

Figure 1 shows the proposed dual-channel graphene TM mode refractive index sensor. The proposed sensor structure is an effective substitute for the conventional Kretschmann configuration, allowing the sensor to excite TM modes in graphene using an oblique incidence of light. A semi-infinite BK7 prism is used as the glass substrate. Light is incident to the prism–graphene layer interface from the prism side using a collinear optical arrangement, which will help to reduce noise and miniaturize the sensor size [41]. The intensity of the reflected light is detected from the same side. The incident light has a wavelength of 633 nm.
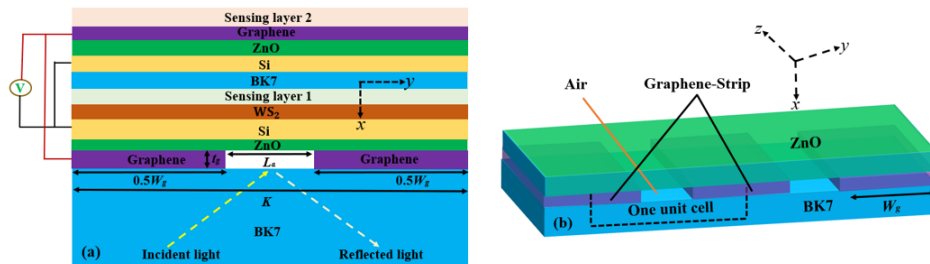
Fig. 1. (a) Two-dimensional (2-D) schematic illustration of the proposed graphene nanostrips TM mode dual-channel refractive index sensor and (b) 3-D schematic view of a part of the proposed sensor that includes the BK7 prism layer, graphene nanostrips, and ZnO.

Graphene nanostrip arrays are placed on the prism material with a separation distance between the strips (L_a) of 100 nm, as shown in Fig. 1. The gaps between the strips are filled with air. Such a structure can be fabricated using the nanoimprint lithography technique as discussed in Ref. [42]. For the purpose of applying voltage, the strips are connected at one end by a conductive strip, as shown in Ref. [43] The air pockets between graphene strips help increase the resonance dip of the reflection profile [44]. The width (W_g) and thickness (t_g) of each graphene nanostrip are 500 nm and 50 nm, respectively. Graphene nanostrips have a periodicity (K) of $K = W_g + L_a = 600$ nm. For numerical analysis, we have considered only one unit cell of the structure with periodic boundary conditions.

In the visible wavelength range, the graphene permittivity (ε_g) can be controlled using a suitable V_g [38]. The ZnO layer used in the proposed sensor between the graphene and Si layers acts as an insulating layer, creating a parallel capacitor model [45]. Such an arrangement can change graphene's optical properties [37]. We apply V_g between Si and graphene to control n_g, E_f, and the electron mobility (μ_g) of graphene [16,45]. The thicknesses of ZnO and Si are 5 nm and 50 nm, respectively. Graphene's optical properties change with V_g, and it can behave like a noble metal in the visible wavelength range with a suitable V_g.

Two-dimensional (2-D) materials like graphene, tungsten diselenide (WSe$_2$), molybdenum disulfide (MoS$_2$), and tungsten disulfide (WS$_2$) can alter the surface characteristics to enhance the adsorption of bio-molecules [46]. We use single-layer WS$_2$ on top of the Si layer for bio-molecule adsorption. The proposed sensor uses two sensing channels. The first one is located on top of the WS$_2$ with a thickness $d_{S1} = 100$ nm [47]. The second sensing layer is on top of the second

graphene layer. The thickness of the second graphene layer is 50 nm. We also assume a thickness $d_{S2} = 100$ nm for the second sensing channel. A 30-nm-thick BK7 glass layer separates the first sensing channel from the Si layer to decrease the reflected light intensity (R). This BK7 layer also acts as the substrate for the second sensing layer arrangement. The first graphene layer consists of nanostrips to help excite the TM modes in graphene. In addition, the periodic array of graphene nanostrips creates a scattering pattern, which illuminates the second graphene layer that acts like a metal [24] and produces TM modes at the second graphene–sensing layer interface.

The different layers of the proposed sensor are two-dimensional except for one of the graphene layers. These layers should be grown without much difficulty using the currently available fabrication techniques. In particular, the graphene layers can be deposited by evaporating atomic carbon in a vacuum using high temperatures [48]. Different dielectric materials can be grown on each other using evaporation or chemical vapor deposition techniques [49]. Nanoimprint lithography can create air gaps between the graphene strips [42]. The first sensing channel in the middle of the layers can be fabricated using a plano-convex singlet lens [50], and a glass flow cell can be used to inject the analyte [51].

3. Optical properties

The performance of the proposed dual-channel refractive index sensor depends on the constituent materials' complex refractive indices. Therefore, the performance of the sensor also depends on the incident wavelength as materials show dispersive optical properties. The refractive index of BK7 prism is wavelength-dependent and can be determined by the method defined in Ref. [52]. The permittivity of the 2-D graphene monolayer is given by [53]

$$\varepsilon_g = 1 + i \frac{\sigma_g}{\omega \varepsilon_0 t_m}, \tag{1}$$

where t_m is the thickness of the graphene monolayer and ε_0 is the free space permittivity. Now, ε_g has two components considering the orientation of the structure, such as tangential and normal. However, for the normal part, an electric field cannot excite any current in the graphene sheet [54].

The optical properties of a few-layer graphene sheet are the same as the monolayer graphene [53]. Generally, σ_g of a graphene sheet is calculated using the Kubo formula [17]

$$\sigma_g = i \frac{e^2 k_B T}{\pi \hbar^2 (\omega + i\tau^{-1})} \left[\frac{E_f}{k_B T} + 2 \ln \left(\exp \left(-\frac{E_f}{k_B T} \right) + 1 \right) \right] + i \frac{e^2}{4\pi\hbar} \ln \left[\frac{2 \mid E_f \mid -\hbar(\omega + i\tau^{-1})}{2 \mid E_f \mid +\hbar(\omega + i\tau^{-1})} \right], \tag{2}$$

where K_B denotes the Boltzmann constant, T denotes the temperature, and e denotes the electron charge. The carrier relaxation time (τ) is related by [37]

$$\tau = \frac{\mu E_f^2}{e v_f}. \tag{3}$$

In this work, we use $v_f = 1.49 \times 10^6$ m/s [43] and determine the Fermi energy as $E_f = \sqrt{\hbar v_f (\pi n_g)}$ [55]. The graphene Fermi energy can be changed by applying V_g. The considered relation can be determined using a parallel-plate capacitor model. The n_g of graphene is determined as $n_g = \varepsilon_r \varepsilon_0 V_g / e d_{ZnO}$ [55]. Here, ε_r is the permittivity of ZnO. We use $\varepsilon_r = 8.5$ for ZnO [56]. Graphene μ_g is given by [57]

$$\mu_g(n_g, T) = \frac{\mu_0}{1 + (n_g/n_{\text{ref}})^A} \times \frac{1}{1 + (T/T_{\text{ref}} - 1)^B}, \tag{4}$$

where $\mu_0 = 225000$ cm^{2}V^{-1}s^{-1}, $n_{\text{ref}} = 1.1 \times 10^{13}$cm^{-2}, $T = 300$ K, $T_{\text{ref}} = 300$ K, $A = 2.2$, and $B = 3$ [57,58]. The intrinsic μ_0 depends on the choice of the substrate, and it can have a value of

$\gtrsim 2 \times 10^5$ cm^{2}V^{-1}s^{-1} with a suitable V_g [58,59]. The refractive indices of ZnO, Si, and WS$_2$ are collected from the literature [60–62]. We use the sample refractive indices from 1.33 to 1.45 for the sensing channels.

4. Simulation method

To determine R-profiles of the proposed dual-channel refractive index sensor, we solve 2-D vectorial Maxwell's equations by the numerical FDTD method. We use the solutions for 2-D configurations as the proposed dual-channel structure is invariant in the z-direction. For 2-D simulations, we set 4000 nm × 600 nm simulation area, including the dual-channel sensing regions. The perfectly matched layer boundary condition is set in the x-direction, and the Bloch boundary condition is in the y-direction.

We have used non-uniform meshing in the simulation area, ensuring a high mesh accuracy and maximum mesh refinement. In our FDTD simulations, the mesh refinement approach obtains sub-cell precision and ensures accuracy for the metal layer and metal–dielectric interface [63]. We have used 1 ns simulation time to converge FDTD calculations. We have used a TM-polarized light source with a 633 nm wavelength. The incidence angle has been varied from 45° to 75° with step size 0.326° to determine the R-profile. The light source is placed in the bottom BK7 region at 1.90 μm from the BK7–graphene interface. We have also recorded the R-profiles using a monitor placed in the same bottom BK7 region at 1.95 μm from the same interface.

5. Dynamics of incident light

The traditional Kretschmann configuration-based sensors obey the following expression [23]

$$\frac{2\pi}{\lambda} n_p \sin\theta_r = \text{Re}\{\beta\}, \tag{5}$$

where λ is the wavelength of the incident light, n_p is the refractive index of the glass prism, θ_r is the resonance angle, and β is the propagation constant of plasmons in graphene. In our dual-channel sensor configuration, the incident light is scattered from the first graphene nanostrip layer. The graphene nanostrip layer creates TM modes with huge wave vectors [24]. The TM modes at the first graphene–sensing layer interface follow the expression [24]

$$\sin\theta_{r1} = \frac{z\lambda}{K\sqrt{\varepsilon_p}}, \tag{6}$$

where ε_p is the permittivity of the prism layer and z is the scattering order. From graphene nanostrips, the dispersed radiation spreads to the second graphene layer through dielectric materials. Hence, TM modes are also created at the second graphene–sensing layer interface, satisfying the following expression [24]

$$\sin\theta_{r2} = \sqrt{\frac{\varepsilon_g \varepsilon_{S2}}{\varepsilon_p(\varepsilon_g + \varepsilon_{S2})}}, \tag{7}$$

where ε_{S2} is the permittivity of the second sensing layer.

6. Results and discussion

Figure 2 shows the optical properties of graphene as functions of V_g for three thicknesses of ZnO. Figure 2(a) shows that n_g increases with V_g. n_g also increases as d_{ZnO} decreases. A similar trend in E_f is observed in Fig. 2(b) with V_g and d_{ZnO}. Alternatively, μ_g decreases when V_g increases, as shown in Fig. 2(c), while μ_g increases as d_{ZnO} increases.

Figure 3 shows ε_g against the light wavelength for different values of d_{ZnO} and V_g. First, we set $V_g = 20$ V and change d_{ZnO}. Figure 3(a) shows the real part of ε_g whereas Fig. 3(b) shows
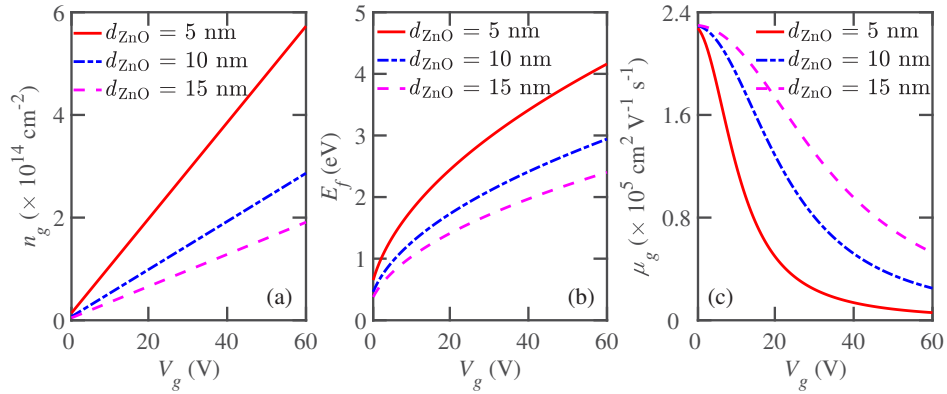
Fig. 2. Optical properties (a) n_g, (b) E_f, and (c) μ_g of the graphene layer as functions of V_g for different thicknesses of ZnO.

the imaginary part for different d_{ZnO}. The real part of ε_g decreases as the wavelength increases. In addition, d_{ZnO} significantly impacts the real part of ε_g. When d_{ZnO} = 5 nm, the real part of ε_g is negative. The negative real part of ε_g confirms the existence of TM modes [12,19]. Furthermore, Im(ε_g) of graphene is almost zero when d_{ZnO} is 5 nm and 10 nm. The real part of ε_g is positive and diverges logarithmically at 545 nm wavelength when d_{ZnO} = 15 nm. The divergent behavior is due to the step-like change of the Im(ε_g), indicating inter-band absorption of radiation at $\hbar\omega > 2E_f$ [12].
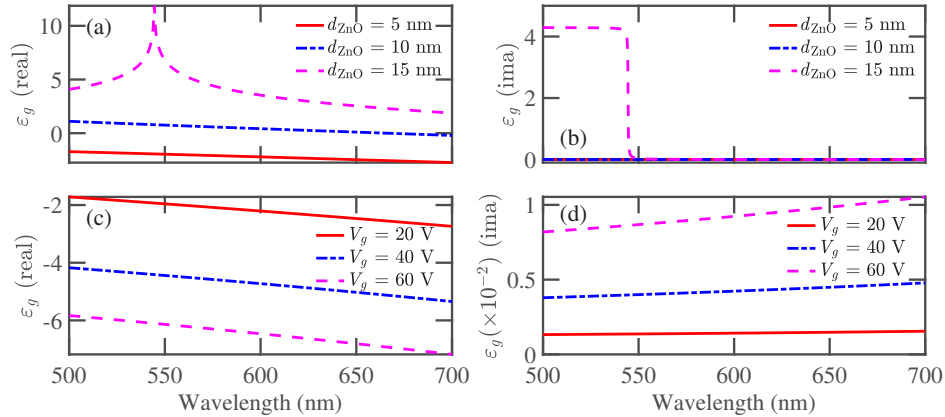

Fig. 3. (a) Real and (b) imaginary parts of the graphene permittivity (ε_g) as a function of the incident light wavelength for different thicknesses of ZnO. The applied gate voltage (V_g) is 20 V in both cases. (c) Real and (d) imaginary parts of (ε_g) as a function of the incident light wavelength for different V_g. The ZnO thickness (d_{ZnO}) is 5 nm in both cases.

Figures 3(c) and 3(d) show ε_g against wavelength for three different V_g, when d_{ZnO} = 5 nm. It is noted that the real part of ε_g becomes more negative as the wavelength increases, as shown in Fig. 3(c). The imaginary part of ε_g has a small value when V_g = 20 V, as shown in Fig. 3(d). However, when V_g = 60 V, the imaginary part of ε_g is also small. Therefore, it is clear that incident wavelength, V_g, and d_{ZnO} have significant influences on ε_g. When d_{ZnO} = 5 nm and V_g = 60 V, $E_f \gg E_p$ in the visible wavelength range, as shown in Fig. 2(b). Therefore, σ_g is dominated by intra-band interactions and can be estimated via the Drude model [64]. At 633 nm

wavelength, the real part of ε_g is negative, and the imaginary part has a nominal value. Hence, graphene acts like a noble metal.

Figure 4 shows the excitation of TM modes in graphene for different V_g. In Fig. 4(a), we show that two TM modes are excited when $V_g = 20$ V. The first TM mode is excited at the BK7–graphene nanostrips–first sensing layer arrangement. The TM mode shows a symmetric behavior, i.e., one mode propagates at the graphene nanostrips–prism interface, and the other propagates between the graphene nanostrips and the first sensing layer arrangement. Scattering patterns are observed as air pockets are present in the graphene nanostrip layer. The scattered light reaches the second graphene layer and excites additional TM modes at the graphene–second sensing layer interface. Figures 4(b) and 4(c) show a similar tendency when $V_g = 40$ V and 60 V, respectively. However, as the negative value of ε_g (real) decreases with an increasing V_g, the excitation of TM modes in the second graphene layer increases with an increasing V_g. We have used $V_g = 60$ V in the results presented in the following analysis. A recent study showed that a single layer of graphene sustained $V_g = 60$ V [37]. As the proposed sensor has many graphene layers, it should be able to withstand the V_g values applied in this work.
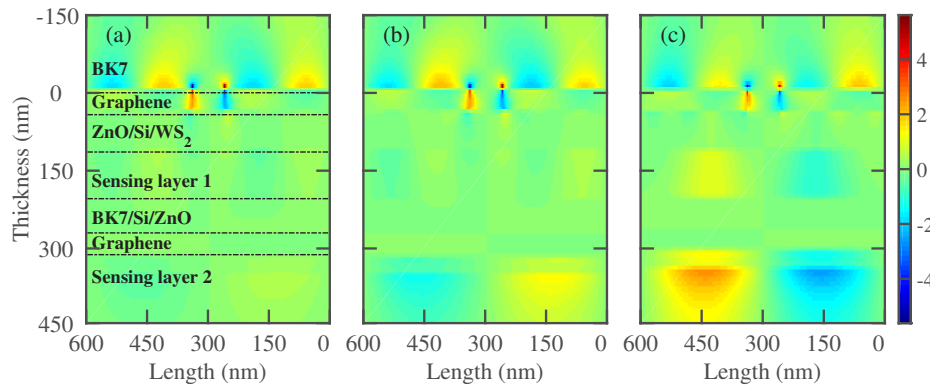

Fig. 4. Excitation of TM modes when $d_{ZnO} = 5$ nm, $n_{S1} = n_{S2} = 1.33$, $L_a = 100$ nm, and $t_g = 50$ nm with (a) $V_g = 20$ V, (b) $V_g = 40$ V, and (c) $V_g = 60$ V.

Figure 5 shows R-profiles as a function of the incident angle (θ_i). As the proposed sensor has dual channels, the same or different sensing materials can be used for the channels. Figure 5(a) shows R-profiles when $n_{S1} = n_{S2} = 1.33$ and $n_{S1} = n_{S2} = 1.36$. In both cases, we observe two resonance dips. When $n_{S1} = n_{S2} = 1.33$, we observe resonances at 49.80° and 67.60°. We consider these two resonance angles as references, θ_{R1} and θ_{R2}, for the first and the second sensing channels. On the other hand, when $n_{S1} = n_{S2} = 1.36$, the first resonance occurs at 50.83° and the second occurs at 70.20°. When $n_{S1} = n_{S2} = 1.36$, the resonance angles shift and the R-profiles widen. At the same time, R_{min} decreases slightly. We note that increasing n_{S1} or n_{S2} increases the light confinement, resulting in a decrease in R_{min}. In addition, increasing n_{S1} or n_{S2} increases the propagation loss of the excited TM modes [38]. Hence, the R-profiles widen.

Figure 5(b) shows the R-profile for different thicknesses of graphene nanostrips. R value decreases when t_g increases. However, when $t_g = 50$ nm, the R value is minimum. When $t_g > 50$ nm, the R value increases, indicating that the absorption of incident light decreases. A similar tendency is observed in Ref. [38]. In Fig. 5(c), we show the R-profile for three different values of L_a. We note that both TM resonances are minimum at $L_a = 100$ nm, confirming the maximum absorption of incident light. Thus, in our proposed sensor, we set $L_a = 100$ nm.

Figures 6(a) and 6(b) show the shifts of θ_{r1} and θ_{r2} for cases when n_{S1} and n_{S2} are the same or different. The shift in θ_{r1} and θ_{r2} increases as n_{S1} or n_{S2} increases. However, θ_{r1} shifts less than θ_{r2}. When $n_{S1} = n_{S2} = 1.45$, maximum value of $\theta_{r1} = 53.88°$ and $\theta_{r2} = 83.27°$ are observed.
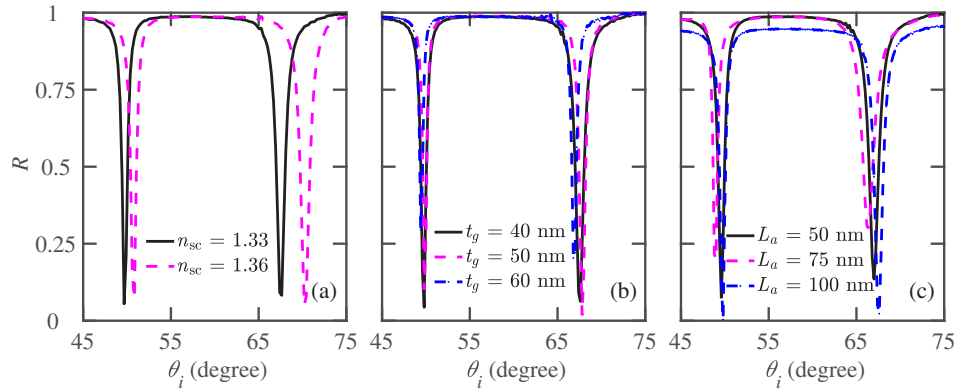
Fig. 5. *R*-profiles of the proposed dual-channel refractive index sensor against the incidence angle for (a) different $n_{S1} = n_{S2} = n_{sc}$ values with $L_a = 100$ nm and $t_g = 50$ nm, (b) different t_g values with $L_a = 100$ nm and $n_{S1} = n_{S2} = 1.33$, and (c) different L_a values with $n_{S1} = n_{S2} = 1.33$ and $t_g = 50$ nm.

The angle shifting property is high when $n_{S1} = 1.35$ to 1.45 and $n_{S2} = 1.42$ to 1.45 for θ_{r1}. Similar tendency is observed when $n_{S1} = 1.37$ to 1.45 and $n_{S2} = 1.41$ to 1.45 for θ_{r2}. We note that the second sensing layer produces greater angle shifts and narrower spectral regions than the first. On the other hand, the proposed dual-channel refractive index sensor can sense two different sensing elements independently. For example, when $n_{S1} = 1.36$ and $n_{S2} = 1.40$, we get $\theta_{r1} = 50.36°$ and $\theta_{r2} = 69.86°$, as shown in Figs. 6(a) and 6(b), respectively.
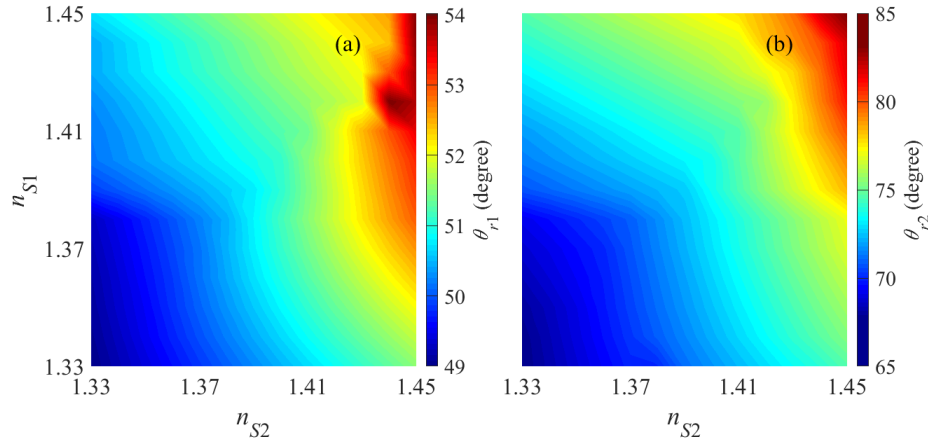

Fig. 6. Resonance angles of the two channels of the proposed sensor (a) θ_{r1} and (b) θ_{r2} as functions of the sensing layers' refractive indices.

Figure 7(a) shows the resonance angle shifting when both channels have the same refractive index. When $n_{S1} = n_{S2} = 1.33$, we find $\theta_{r1} = 49.80°$ and $\theta_{r2} = 67.60°$, respectively. Next, when $n_{S1} = n_{S2} = 1.34$, we get $\theta_{r1} = 49.99°$ and $\theta_{r2} = 67.91°$. We calculate the sensitivities of the channels by $S_1 = \Delta\theta_{r1}/\Delta n_{S1}$ and $S_2 = \Delta\theta_{r2}/\Delta n_{S2}$. Figure 7(b) shows the combined sensitivity when both sensing channels have the same refractive index. The combined sensitivity (S) of the proposed dual-channel sensor is calculated by multiplying the sensitivities of the individual channels as given by

$$S = S_1 S_2. \tag{8}$$

Therefore, when $n_{S1} = n_{S2} = 1.34$, $S = 1645$ degrees/RIU. Increasing n_{S1} and n_{S2} with $n_{S1} = n_{S2}$ increases S as well. When $n_{S1} = n_{S2} = 1.45$, S is the maximum with a value of 2530 degrees/RIU.
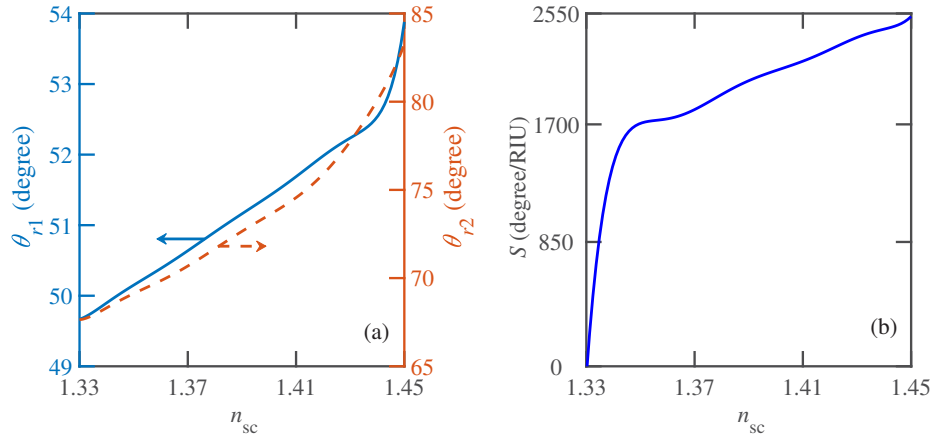

Fig. 7. (a) Resonance angles θ_{r1} and θ_{r2} against the same refractive index ($n_{S1} = n_{S2} = n_{sc}$) in both channels. (b) Sensitivity (S) against the same refractive index ($n_{S1} = n_{S2} = n_{sc}$) in both channels.

Figure 8 shows the sensitivity of the proposed sensor when n_{S1} and n_{S2} vary. Figure 8(a) shows the sensitivity of the first sensing channel, and Fig. 8(b) shows that of the second. We calculate the sensitivities of the first and second sensing channels using $S_1 = (\theta_{r1} - \theta_{R1})/(n_{S1} - 1.33)$ and $S_2 = (\theta_{r2} - \theta_{R2})/(n_{S2} - 1.33)$, respectively. Both sensing channels' sensitivity is the maximum when $n_{S1} = 1.340$–1.355 and $n_{S2} = 1.40$–1.45. We find $S_1 = 236$ degrees/RIU and $S_2 = 773$ degrees/RIU in a narrow refractive index region, which will help detect specific analytes with refractive index in this region with high sensitivity. Such high sensitivity in a narrow refractive index region has also been observed in Ref. [65]. In addition, the second sensing channel shows ~3.25 times higher sensitivity than the first and significantly higher than the existing literature [52,66–69]. Recently, adjustable dual plasmons have been shown using single-layer graphene in the THz region, where the sensitivities are 0.92 THz/RIU and 1.08 THz/RIU for the first and the second transmission peaks, respectively [70]. We have compared our results with the existing literature in Table 1. For comparison, we have considered sensors that use 2-D graphene and operate at 633 nm incident wavelength.

Table 1. Performance comparison of our proposed sensor with different recently reported sensors.

Sensor configuration	S (degree/RIU)
Prism /Al /Au /Graphene /WSe$_2$ /Sensing layer [32]	164
Prism /ZnO /Ag /BaTiO$_3$ /Graphene /Sensing layer [71]	157
Prism /Au /PtSe$_2$ /Graphene /Sensing layer [72]	154
Prism /Ag /2-D materials /Graphene /Sensing layer [73]	210
This work (first sensing layer)	236
This work (second sensing layer)	773
This work (two sensing layers with the same analyte)	2530

We note that the 50-nm-thick graphene layer used in the proposed sensor will have many graphene monolayers. Researchers have recently demonstrated 100- and 200-nm-thick graphene
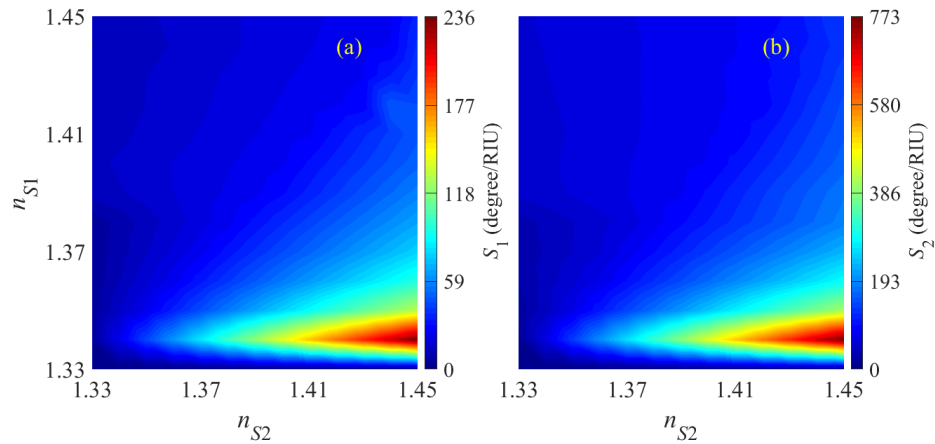
Fig. 8. Sensitivities of the proposed sensor (a) S_1 and (b) S_2 against refractive index variations of the two channels.

layers [74,75]. Graphene's optical properties are characterized by surface conductivity rather than volumetric permittivity. Bodepudi et al. showed that the conductivity of graphene could be modeled for a single layer and used to represent multiple layers by scaling the total conductivity by the number of layers [75]. Therefore, a ~200-nm-thick graphene layer should behave similarly to monolayer or few-layer graphene. A 50-nm-thick graphene layer can be fabricated following the manufacturing process discussed in Ref. [74] or [75] and have monolayer-like optical properties. In addition, we have simulated the proposed structure using a graphene layer thickness of 3.4 nm, which is equivalent to only 10 graphene monolayers. The responses of the proposed sensor remain the same qualitatively, with a slight ($\lesssim 5\%$) quantitative change. However, the sensor performance may significantly change if a 50-nm-thick graphite layer replaces the graphene layer.

7. Conclusion

We show that the unusual TM modes in graphene at visible wavelength can be excited using the proposed modified Kretschmann configuration without needing noble metal. Our proposed graphene nanostrips-based plasmonic sensor produces TM modes between graphene nanostrips and the first sensing layer. These nanostrips also scatter the incoming incidence light with a large propagating wave vector, producing another TM mode in the graphene–second sensing layer interface. The creation of TM modes depends on several factors, such as the gate voltage, incident wavelength, and thickness of ZnO. The proposed dual-channel refractive index sensor is highly sensitive when both channels have the same refractive index. In addition, it can detect refractive indices of the sensing channels separately using the two resonance dips. The structural and material properties used in the proposed sensor are conceivable and can easily be fabricated.

References

1. W. L. Barnes, A. Dereux, and T. W. Ebbesen, "Surface plasmon subwavelength optics," Nature **424**(6950), 824–830 (2003).
2. F. Ramos-Mendieta, J. Hernández-López, and M. Palomino-Ovando, "Transverse magnetic surface plasmons and complete absorption supported by doped graphene in otto configuration," AIP Adv. **4**(6), 067125 (2014).
3. X. Y. He and R. Li, "Comparison of graphene-based transverse magnetic and electric surface plasmon modes," IEEE J. Sel. Top. Quantum Electron. **20**(1), 62–67 (2014).

4. N. Zhang, W. Luo, L. Wang, J. Fan, W. Wu, M. Ren, X. Zhang, W. Cai, and J. Xu, "Strong in-plane scattering of acoustic graphene plasmons by surface atomic steps," Nat. Commun. **13**(1), 983 (2022).

5. L. Cui, J. Wang, and M. Sun, "Graphene plasmon for optoelectronics," Rev. Phys. **6**, 100054 (2021).

6. I. Epstein, D. Alcaraz, Z. Huang, V.-V. Pusapati, J.-P. Hugonin, A. Kumar, X. M. Deputy, T. Khodkov, T. G. Rappoport, J.-Y. Hong, N. M. R. Peres, J. Kong, D. R. Smith, and F. H. Koppens, "Far-field excitation of single graphene plasmon cavities with ultracompressed mode volumes," Science **368**(6496), 1219–1223 (2020).

7. A. Woessner, Y. Gao, I. Torre, M. B. Lundeberg, C. Tan, K. Watanabe, T. Taniguchi, R. Hillenbrand, J. Hone, M. Polini, and F. H. L. Koppens, "Electrical 2π phase control of infrared light in a 350-nm footprint using graphene plasmons," Nat. Photonics **11**(7), 421–424 (2017).

8. Z. Fei, A. Rodin, G. O. Andreev, W. Bao, A. McLeod, M. Wagner, L. Zhang, Z. Zhao, M. Thiemens, G. Dominguez, M. M. Fogler, A. H. C. Neto, C. N. Lau, F. Keilmann, and D. N. Basov, "Gate-tuning of graphene plasmons revealed by infrared nano-imaging," Nature **487**(7405), 82–85 (2012).

9. F. Wang, Y. Zhang, C. Tian, C. Girit, A. Zettl, M. Crommie, and Y. R. Shen, "Gate-variable optical transitions in graphene," Science **320**(5873), 206–209 (2008).

10. D. R. Mason, S. G. Menabde, S. Yu, and N. Park, "Plasmonic excitations of 1d metal-dielectric interfaces in 2d systems: 1d surface plasmon polaritons," Sci. Rep. **4**(1), 4536 (2014).

11. S. G. Menabde, D. R. Mason, E. E. Kornev, C. Lee, and N. Park, "Direct optical probing of transverse electric mode in graphene," Sci. Rep. **6**(1), 21523 (2016).

12. S. A. Mikhailov and K. Ziegler, "New electromagnetic mode in graphene," Phys. Rev. Lett. **99**(1), 016803 (2007).

13. O. Kotov, M. Kol'chenko, and Y. E. Lozovik, "Ultrahigh refractive index sensitivity of te-polarized electromagnetic waves in graphene at the interface between two dielectric media," Opt. Express **21**(11), 13533–13546 (2013).

14. N. K. Emani, A. V. Kildishev, V. M. Shalaev, and A. Boltasseva, "Graphene: a dynamic platform for electrical control of plasmonic resonance," Nanophotonics **4**(1), 214–223 (2015).

15. H. Jiang, W. Zhao, and Y. Jiang, "High-efficiency tunable circular asymmetric transmission using dielectric metasurface integrated with graphene sheet," Opt. Express **25**(17), 19732–19739 (2017).

16. J. Hu, Y. Qing, S. Yang, Y. Ren, X. Wu, W. Gao, and C. Wu, "Tailoring total absorption in a graphene monolayer covered subwavelength multilayer dielectric grating structure at near-infrared frequencies," J. Opt. Soc. Am. B **34**(4), 861–868 (2017).

17. G. W. Hanson, "Dyadic green's functions and guided surface waves for a surface conductivity model of graphene," J. Appl. Phys. **103**(6), 064302 (2008).

18. D. A. Kuzmin, I. V. Bychkov, V. G. Shavrov, and L. N. Kotov, "Transverse-electric plasmonic modes of cylindrical graphene-based waveguide at near-infrared and visible frequencies," Sci. Rep. **6**(1), 26915 (2016).

19. T. M. Wijesinghe, M. Premaratne, and G. P. Agrawal, "Low-loss dielectric-loaded graphene surface plasmon polariton waveguide based biochemical sensor," J. Appl. Phys. **117**(21), 213105 (2015).

20. L. Ju, B. Geng, J. Horng, C. Girit, M. Martin, Z. Hao, H. A. Bechtel, X. Liang, A. Zettl, Y. R. Shen, and F. Wang, "Graphene plasmonics for tunable terahertz metamaterials," Nat. Nanotechnol. **6**(10), 630–634 (2011).

21. X. Zhu, W. Yan, P. Uhd Jepsen, O. Hansen, N. Asger Mortensen, and S. Xiao, "Experimental observation of plasmons in a graphene monolayer resting on a two-dimensional subwavelength silicon grating," Appl. Phys. Lett. **102**(13), 131101 (2013).

22. H. Lu, B. P. Cumming, and M. Gu, "Highly efficient plasmonic enhancement of graphene absorption at telecommunication wavelengths," Opt. Lett. **40**(15), 3647–3650 (2015).

23. D.-W. Huang, Y.-F. Ma, M.-J. Sung, and C.-P. Huang, "Approach the angular sensitivity limit in surface plasmon resonance sensors with low index prism and large resonant angle," Opt. Eng. **49**(5), 054403 (2010).

24. M. H. Elshorbagy, A. Cuadrado, and J. Alda, "High-sensitivity integrated devices based on surface plasmon resonance for sensing applications," Photonics Res. **5**(6), 654–661 (2017).

25. M. Sun, T. Sun, Y. Liu, L. Zhu, F. Liu, Y. Huang, and C. Chang-Hasnain, "Integrated plasmonic refractive index sensor based on grating/metal film resonant structure," in *High Contrast Metastructures V*, vol. 9757 (SPIE, 2016), pp. 86–91.

26. L. Li, Y. Liang, J. Guang, W. Cui, X. Zhang, J.-F. Masson, and W. Peng, "Dual kretschmann and otto configuration fiber surface plasmon resonance biosensor," Opt. Express **25**(22), 26950–26957 (2017).

27. H. Jiang, S. Choudhury, Z. A. Kudyshev, D. Wang, L. J. Prokopeva, P. Xiao, Y. Jiang, and A. V. Kildishev, "Enhancing sensitivity to ambient refractive index with tunable few-layer graphene/hbn nanoribbons," Photonics Res. **7**(7), 815–822 (2019).

28. T. Cao and L. Zhang, "Enhancement of fano resonance in metal/dielectric/metal metamaterials at optical regime," Opt. Express **21**(16), 19228–19239 (2013).

29. A. Dhawan, M. Canva, and T. Vo-Dinh, "Narrow groove plasmonic nano-gratings for surface plasmon resonance sensing," Opt. Express **19**(2), 787–813 (2011).

30. A. Bijalwan and V. Rastogi, "Sensitivity enhancement of a conventional gold grating assisted surface plasmon resonance sensor by using a bimetallic configuration," Appl. Opt. **56**(35), 9606–9612 (2017).

31. F.-C. Chien and S.-J. Chen, "A sensitivity comparison of optical biosensors based on four different surface plasmon resonance modes," Biosens. Bioelectron. **20**(3), 633–642 (2004).

32. A. Bijalwan, B. K. Singh, and V. Rastogi, "Surface plasmon resonance-based sensors using nano-ribbons of graphene and wse2," Plasmonics **15**(4), 1015–1023 (2020).

33. H. Cai, M. Wang, J. Liu, and X. Wang, "Theoretical and experimental study of a highly sensitive spr biosensor based on au grating and au film coupling structure," Opt. Express **30**(15), 26136–26148 (2022).

34. C. How Gan, "Analysis of surface plasmon excitation at terahertz frequencies with highly doped graphene sheets via attenuated total reflection," Appl. Phys. Lett. **101**(11), 111609 (2012).

35. Y. V. Bludov, M. I. Vasilevskiy, and N. M. Peres, "Tunable graphene-based polarizer," J. Appl. Phys. **112**(8), 084320 (2012).

36. Y. V. Bludov, N. M. Peres, and M. I. Vasilevskiy, "Unusual reflection of electromagnetic radiation from a stack of graphene layers at oblique incidence," J. Opt. **15**(11), 114004 (2013).

37. H. Lu, C. Zeng, Q. Zhang, X. Liu, M. M. Hossain, P. Reineck, and M. Gu, "Graphene-based active slow surface plasmon polaritons," Sci. Rep. **5**(1), 8443 (2015).

38. M. M. Hossain and M. A. Talukder, "Gate-controlled graphene surface plasmon resonance glucose sensor," Opt. Commun. **493**, 126994 (2021).

39. D. K. Efetov and P. Kim, "Controlling electron-phonon interactions in graphene at ultrahigh carrier densities," Phys. Rev. Lett. **105**(25), 256805 (2010).

40. W. M. Haynes, *CRC Handbook of Chemistry and Physics* (CRC press, 2014).

41. A. K. Sharma and A. K. Pandey, "Self-referenced plasmonic sensor with tio2 grating on thin au layer: simulated performance analysis in optical communication band," J. Opt. Soc. Am. B **36**(8), F25–F31 (2019).

42. B. Erenturk, M.-H. Park, V. M. Rotello, and K. R. Carter, "Fabrication of air gap dielectrics by nanoimprint lithography," Microelectron. Eng. **98**, 89–96 (2012).

43. C. Hwang, D. A. Siegel, S.-K. Mo, W. Regan, A. Ismach, Y. Zhang, A. Zettl, and A. Lanzara, "Fermi velocity engineering in graphene by substrate modification," Sci. Rep. **2**(1), 590 (2012).

44. Z. Yu and S. Fan, "Extraordinarily high spectral sensitivity in refractive index sensors using multiple optical modes," Opt. Express **19**(11), 10029–10040 (2011).

45. Y. Yin, Z. Cheng, L. Wang, K. Jin, and W. Wang, "Graphene, a material for high temperature devices–intrinsic carrier density, carrier drift velocity, and lattice energy," Sci. Rep. **4**(1), 5758 (2014).

46. Z. Lin, S. Chen, and C. Lin, "Sensitivity improvement of a surface plasmon resonance sensor based on two-dimensional materials hybrid structure in visible region: A theoretical study," Sensors **20**(9), 2445 (2020).

47. S. Pal, A. Verma, J. P. Saini, and Y. K. Prajapati, "Sensitivity enhancement using silicon-black phosphorus-tdmc coated surface plasmon resonance biosensor," IET Optoelectron. **13**(4), 196–201 (2019).

48. A. Panda, P. D. Pukhrambam, and G. Keiser, "Performance analysis of graphene-based surface plasmon resonance biosensor for blood glucose and gas detection," Appl. Phys. A **126**(3), 153 (2020).

49. C.-W. Lin, K.-P. Chen, C.-N. Hsiao, S. Lin, and C.-K. Lee, "Design and fabrication of an alternating dielectric multi-layer device for surface plasmon resonance sensor," Sens. Actuators, B **113**(1), 169–176 (2006).

50. Y. Kaneoka, K. Nishigaki, Y. Mizutani, and T. Iwata, "Precise measurement of the thickness of a dielectric layer on a metal surface by use of a modified otto optical configuration," Int. J. Optomechatronics **9**(1), 48–61 (2015).

51. R. Nasirifar, M. Danaie, and A. Dideban, "Dual channel optical fiber refractive index sensor based on surface plasmon resonance," Optik **186**, 194–204 (2019).

52. P. Sun, M. Wang, L. Liu, L. Jiao, W. Du, F. Xia, M. Liu, W. Kong, L. Dong, and M. Yun, "Sensitivity enhancement of surface plasmon resonance biosensor based on graphene and barium titanate layers," Appl. Surf. Sci. **475**, 342–347 (2019).

53. A. Al Sayem, M. R. C. Mahdy, I. Jahangir, and M. S. Rahman, "Ultrathin ultra-broadband electro-absorption modulator based on few-layer graphene based anisotropic metamaterial," Opt. Commun. **384**, 50–58 (2017).

54. B. Zhu, G. Ren, S. Zheng, Z. Lin, and S. Jian, "Nanoscale dielectric-graphene-dielectric tunable infrared waveguide with ultrahigh refractive indices," Opt. Express **21**(14), 17089–17096 (2013).

55. W. Gao, J. Shu, C. Qiu, and Q. Xu, "Excitation of plasmonic waves in graphene by guided-mode resonances," ACS Nano **6**(9), 7806–7813 (2012).

56. S. V. Vegesna, V. J. Bhat, D. Bürger, J. Dellith, I. Skorupa, O. G. Schmidt, and H. Schmidt, "Increased static dielectric constant in znmno and zncoo thin films with bound magnetic polarons," Sci. Rep. **10**(1), 6698 (2020).

57. V. E. Dorgan, M.-H. Bae, and E. Pop, "Mobility and saturation velocity in graphene on Sio$_2$," Appl. Phys. Lett. **97**(8), 082112 (2010).

58. J.-H. Chen, C. Jang, S. Xiao, M. Ishigami, and M. S. Fuhrer, "Intrinsic and extrinsic performance limits of graphene devices on SiO$_2$," Nat. Nanotechnol. **3**(4), 206–209 (2008).

59. C. Berger, Z. Song, X. Li, X. Wu, N. Brown, C. Naud, D. Mayou, T. Li, J. Hass, A. N. Marchenkov, E. H. Conrad, P. N. First, and W. A. de Heer, "Electronic confinement and coherence in patterned epitaxial graphene," Science **312**(5777), 1191–1196 (2006).

60. A. S. Kushwaha, A. Kumar, R. Kumar, and S. Srivastava, "A study of surface plasmon resonance (SPR) based biosensor with improved sensitivity," Photonics Nanostructures-Fundamentals Appl. **31**, 99–106 (2018).

61. D. E. Aspnes and A. Studna, "Dielectric functions and optical parameters of Si, Ge, GaP, GaAs, GaSb, InP, InAs, and InsS from 1.5 to 6.0 ev," Phys. Rev. B **27**(2), 985–1009 (1983).

62. M. S. Rahman, M. R. Hasan, K. A. Rikta, and M. Anower, "A novel graphene coated surface plasmon resonance biosensor with tungsten disulfide (ws$_2$) for sensing dna hybridization," Opt. Mater. **75**, 567–573 (2018).

63. W. Yu and R. Mittra, "A conformal finite difference time domain technique for modeling curved dielectric surfaces," IEEE Microw. Wireless Compon. Lett. **11**(1), 25–27 (2001).

Optical Materials EXPRESS

64. Y. Huang, S. Zhong, H. Yao, and D. Cui, "Tunable terahertz plasmonic sensor based on graphene/insulator stacks," IEEE Photonics J. **9**(1), 1–10 (2017).

65. Y. Xu, L. Wu, and L. K. Ang, "Mos2-based highly sensitive near-infrared surface plasmon resonance refractive index sensor," IEEE J. Sel. Top. Quantum Electron. **25**(2), 1–7 (2019).

66. X. Dai, Y. Liang, Y. Zhao, S. Gan, Y. Jia, and Y. Xiang, "Sensitivity enhancement of a surface plasmon resonance with tin selenide (snse) allotropes," Sensors **19**(1), 173 (2019).

67. Y. Jia, Y. Liao, and H. Cai, "Sensitivity improvement of surface plasmon resonance biosensors with Ges-metal layers," Electronics **11**(3), 332 (2022).

68. S. Singh, A. K. Sharma, P. Lohia, and D. Dwivedi, "Theoretical analysis of sensitivity enhancement of surface plasmon resonance biosensor with zinc oxide and blue phosphorus/mos2 heterostructure," Optik **244**, 167618 (2021).

69. L. Wu, Y. Xiang, and Y. Qin, "Ch3nh3pbbr3 thin film served as guided-wave layer for enhancing the angular sensitivity of plasmon biosensor," Biosensors **11**(11), 415 (2021).

70. J. Ge, C. You, H. Feng, X. Li, M. Wang, L. Dong, G. Veronis, and M. Yun, "Tunable dual plasmon-induced transparency based on a monolayer graphene metamaterial and its terahertz sensing performance," Opt. Express **28**(21), 31781–31795 (2020).

71. A. Kumar, A. K. Yadav, A. S. Kushwaha, and S. Srivastava, "A comparative study among WS2, MoS2 and graphene based surface plasmon resonance (SPR) sensor," Opt. Express **2**(1), 100015 (2020).

72. T. B. A. Akib, S. F. Mou, M. M. Rahman, M. M. Rana, M. R. Islam, I. M. Mehedi, M. P. Mahmud, and A. Z. Kouzani, "Design and numerical analysis of a graphene-coated spr biosensor for rapid detection of the novel coronavirus," Sensors **21**(10), 3491 (2021).

73. M. M. Hossain and M. A. Talukder, "Graphene surface plasmon sensor for ultra-low-level sars-cov-2 detection," PLoS One **18**(4), e0284812 (2023).

74. J.-H. Lee, P. E. Loya, J. Lou, and E. L. Thomas, "Dynamic mechanical behavior of multilayer graphene via supersonic projectile penetration," Science **346**(6213), 1092–1096 (2014).

75. S. C. Bodepudi, A. P. Singh, and S. Pramanik, "Giant current-perpendicular-to-plane magnetoresistance in multilayer graphene as grown on nickel," Nano Lett. **14**(5), 2233–2241 (2014).